

Realistic Simulations of the Galactic Polarized Foreground: Consequences for 21-cm Reionization Detection Experiments

Vibor Jelić^{1,2*}, Saleem Zaroubi¹, Panagiotis Labropoulos¹, Gianni Bernardi³,
A. G. de Bruyn^{1,2} and Léon V. E. Koopmans¹

¹*Kapteyn Astronomical Institute, University of Groningen, P.O. Box 800, 9700 AV Groningen, the Netherlands*

²*ASTRON, P.O. Box 2, 7990 AA Dwingeloo, the Netherlands*

³*Harvard Smithsonian Center for Astrophysics, 60 Garden Street, Cambridge, MA 02138, USA*

15 May 2022

ABSTRACT

Experiments designed to measure the redshifted 21 cm line from the Epoch of Reionization (EoR) are challenged by strong astrophysical foreground contamination, ionospheric distortions, complex instrumental response and other different types of noise (e.g. radio frequency interference). The astrophysical foregrounds are dominated by diffuse synchrotron emission from our Galaxy. Here we present a simulation of the Galactic emission used as a foreground module for the LOFAR- EoR key science project end-to-end simulations. The simulation produces total and polarized intensity over $10^\circ \times 10^\circ$ maps of the Galactic synchrotron and free-free emission, including all observed characteristics of the emission: spatial fluctuations of amplitude and spectral index of the synchrotron emission, together with Faraday rotation effects. The importance of these simulations arise from the fact that the Galactic polarized emission could behave in a manner similar to the EoR signal along the frequency direction. As a consequence, an improper instrumental calibration will give rise to leakages of the polarized to the total signal and mask the desired EoR signal. In this paper we address this for the first time through realistic simulations.

Key words: cosmology: theory, diffuse radiation, observation; radio lines: general; instrumentation: interferometers; radio continuum: general

1 INTRODUCTION

The Epoch of Reionization (EoR) is expected to occur between redshift 6 and 12, as indicated from observed cosmic microwave background (CMB) polarization (Komatsu et al. 2009), high redshift quasar spectra (Fan et al. 2006), and the thermal history of of the intergalactic medium (Theuns et al. 2002a,b; Bolton et al. 2010). At redshifts, the 21 cm line from neutral hydrogen is shifted into meter wavelengths and therefore sets the frequency range of EoR experiments to the long-wavelength part of the radio spectrum ($\sim 100 - 200$ MHz).

There are several planned and ongoing experiments designed to probe the EoR through redshifted 21 cm emission line from neutral hydrogen using radio arrays: GMRT¹, LOFAR², MWA³, 21CMA⁴, PAPER⁵, and SKA⁶.

The low-frequency radio sky at these wavelengths is dominated by diffuse synchrotron emission from the Galaxy and integrated emission from extragalactic sources (radio galaxies and clusters). Although, this foreground emission is 4 – 5 orders of magnitude stronger than the expected EoR signal, the ratio between their intensity fluctuations on arcmin to degree scales measured by interferometers is ‘only’ 2 – 3 orders of magnitude (Shaver et al. 1999). In addition to the foregrounds, the EoR experiments are also challenged by understanding of the instrumental response and ionospheric disturbances to high precision (Labropoulos, in preparation).

Currently there are numerous efforts to simulate all the data components of the EoR experiments: cosmological 21 cm signal, foregrounds, ionosphere and instrumental response. The main aim of these end to end simulations is to develop a robust signal extraction scheme for the extremely challenging EoR observations (e.g. Santos et al. 2005; Morales et al. 2006; Wang et al. 2006; Jelić et al. 2008; Bowman et al. 2009; Harker et al. 2009a,b; Labropoulos et al. 2009).

The foregrounds in the context of the EoR measurements have been studied theoretically by various authors. Shaver et al. (1999) have given the first overview of the foreground components. Di

* E-mail: vjelic@astro.rug.nl

¹ Giant Metrewave Telescope, <http://gmrt.ncra.tifr.res.in>

² Low Frequency Array, <http://www.lofar.org>

³ Murchinson Widefield Array, <http://www.mwatelescope.org/>

⁴ 21 Centimeter Array, <http://21cma.bao.ac.cn/>

⁵ Precision Array to Probe EoR, <http://astro.berkeley.edu/~dbacker/eor>

⁶ Square Kilometer Array, <http://www.skatelescope.org/>

Matteo et al. (2002, 2004) have studied emission from unresolved extragalactic sources at low radio frequencies. Oh & Mack (2003) and Cooray (2004) have considered the effect of free-free emission from extragalactic haloes. Santos et al. (2005) carried out a detailed study of the functional form of the foreground correlations. Jelić et al. (2008) have made the first detailed foreground model and have simulated the maps that include both the diffuse emission from our Galaxy and extragalactic sources (radio galaxies and clusters). Gleser et al. (2008) have also studied both galactic and extragalactic foregrounds. de Oliveira-Costa et al. (2008) has used all publicly available total power radio surveys to obtain all-sky Galactic maps at the desired frequency range and Bowman et al. (2009) has studied foreground contamination in the context of the power spectrum estimation.

Recently, a Galactic 3D emission model has been developed by Sun et al. (2008); Waelkens et al. (2009); Sun & Reich (2009) (the HAMMURABI⁷ code), derived from a 3D distribution of the Galactic thermal electrons, cosmic-ray electrons and magnetic fields. The code is able to reproduce all-sky or zoom-in maps of the Galactic emission over a wide frequency range.

In addition to simulations, a number of observational projects have given estimates of Galactic foregrounds in small selected areas. Ali et al. (2008) have used 153 MHz observations with GMRT to characterize the visibility correlation function of the foregrounds. Rogers & Bowman (2008) have measured the spectral index of the diffuse radio background between 100 and 200 MHz. Pen et al. (2009) have set an upper limit to the diffuse polarized Galactic emission; and Bernardi et al. (2009, 2010) obtained the most recent and comprehensive targeted observations with the Westerbork Synthesis Radio Telescope (WSRT).

However, current observations are not able to fully constrain the foregrounds, especial the Galactic polarized synchrotron emission, as required by EoR experiments. The importance of the polarized foreground stems from the fact that the LOFAR instrument, in common with all current interferometric EoR experiments, has an instrumentally polarized response. An improper polarization calibration will give rise to leakages of the complex polarized signal to the total signal. Since the Galactic polarized emission is quite structured along the frequency direction, the leakage of polarized intensity will have similar structures along the frequency and will mimic the EoR signal. Therefore, for reliable detection of the EoR signal it is essential at this stage: (i) to simulate the polarized foregrounds, and (ii) to test the influence of the leakages on the extraction of the EoR signal. This paper focuses on both aspects.

In our previous foreground model (Jelić et al. 2008), the total intensity Galactic emission maps were obtained from three Gaussian random fields. The first two were for the amplitudes of synchrotron and free-free emission and the third was for the spectral index of the synchrotron emission. The polarized maps were simulated in a similar way but with added multiple 2D Faraday screens along the line of sight. Despite the ability of that model to simulate observed characteristics of the Galactic emission (e.g. spatial and frequency variations of brightness temperature and its spectral index), the model had some disadvantages: e.g. the Galactic emission was derived *ad hoc* and depolarization effects were not taken into account.

Our new foreground model, presented in this paper, is an extension of our previous foreground model (Jelić et al. 2008). It simulates both Galactic synchrotron and free-free emission in total

and polarized intensity, but in a more realistic way and with some additional benefits. The Galactic emission in our current model is derived from the physical quantities and 3D characteristics of the Galaxy (the cosmic ray and thermal electron density, and the magnetic field; e.g. Beck et al. 1996; Berkhuijsen et al. 2006; Sun et al. 2008, and references therein). In addition, the model has the flexibility to simulate any peculiar case of the Galactic emission including very complex 3D polarized structures produced by “Faraday screens” and depolarization due to Faraday thick layers.

Our Galactic emission model has some similarities with the HAMMURABI model, but the difference between the two is the main purpose of the simulations. The HAMMURABI simulation is based on a very complex Galactic model with aim to reproduce the observed all-sky maps of the Galactic emission. Because of its complexity, the high resolution zoom-in maps require a lot of computing power and time (Sun & Reich 2009). In contrast, our model is restricted to produce fast and relatively small maps of Galactic emission, which are then used as a foreground template for the LOFAR-EoR end to end simulation. Since the foreground subtraction is usually done along the frequency direction, our model also includes 3D spatial variations of the spectral index of the Galactic synchrotron radiation.

The paper is organized as follows. Section 2 gives a brief theoretical overview of the Galactic emission and Faraday rotation. The observational constrains of the Galactic emission are presented in Sec. 3. The simulation algorithm is described in Sec. 4, while a few examples of simulated maps of the Galactic emission are presented in Sec. 5. Section 5 also give a quantitative comparison of our simulations with the observations. Section 6 describes the EoR signal and instrumental response simulations of the LOFAR-EoR pipeline. We discuss the influence of the polarized foregrounds on the extraction of the EoR in Sec. 7. The paper concludes with summary and conclusions (Sec. 8).

2 THEORY

In radio astronomy, at frequencies where the Rayleigh-Jeans law is applicable, the radiation intensity, I (energy emitted per unit time per solid angle and per unit area and unit frequency), at the frequency ν is commonly expressed in terms of the brightness temperature (T_b):

$$T_b(\nu) = \frac{c^2}{2k_B\nu^2} I(\nu), \quad (1)$$

where c is the speed of light and k_B Boltzmann’s constant.

The emission coefficient, j (energy emitted per unit time per solid angle and per unit volume), at a certain frequency can also be expressed in terms of the unit temperature, $j_b(\nu) = \frac{c^2}{2k_B\nu^2} j(\nu)$, so that:

$$T_b(\nu) = \int j_b(\nu) ds, \quad (2)$$

where the integral is taken along the line of sight (LOS).

In the following subsection we will give a brief theoretical overview of the Galactic synchrotron and free-free emission, as well as Faraday rotation, that will be used later in the simulation. The Galactic emission will be expressed in terms of j_b and T_b .

2.1 Synchrotron emission

Synchrotron emission originates from the interaction between relativistically moving charges and magnetic fields. In our own galaxy,

⁷ <http://www.mpa-garching.mpg.de/hammurabi/>

synchrotron emission arises from cosmic ray (CR) electrons produced mostly by supernova explosions and the Galactic magnetic field. A fairly complete exposition of the synchrotron emission theory is presented in e.g. Pacholczyk (1970) and Rybicki & Lightman (1986). Here we only give a simple description of the emission.

The Galactic synchrotron emission is partially linearly polarized. Its properties depend on the spatial and energy distribution of the CR electrons, and the strength and orientation of the perpendicular (with respect to the LOS) component of the Galactic magnetic field, B_{\perp} . The emission coefficients of the Galactic total and polarized synchrotron radiation, j_b^{Isyn} and j_b^{PIsyn} , are given respectively in *cgs* units, at the frequency ν , by:

$$j_b^{I,PIsyn} = C_{I,PIsyn} \left(\frac{2\pi m_e c}{3e} \right)^{-\frac{p-1}{2}} n_{CR} B_{\perp}^{\frac{p+1}{2}} \nu^{-\frac{p+3}{2}}, \quad (3)$$

with

$$C_{Isyn} = \frac{\sqrt{3}e^3}{8\pi m_e k_B (p+1)} \Gamma\left(\frac{p}{4} - \frac{1}{12}\right) \Gamma\left(\frac{p}{4} + \frac{19}{12}\right), \quad (4)$$

$$C_{PIsyn} = \frac{\sqrt{3}e^3}{32\pi m_e k_B} \Gamma\left(\frac{p}{4} - \frac{1}{12}\right) \Gamma\left(\frac{p}{4} + \frac{7}{12}\right). \quad (5)$$

The charge of the electron is given by $e = 4.8 \cdot 10^{-10}$ Fr, the mass by $m_e = 9.1 \cdot 10^{-28}$ g and n_{CR} is the CR electron density. Note that for the CR electrons we assume that their energy spectrum is a power law with a spectral index p : $N(\gamma)d\gamma = n_{CR0}\gamma^{-p}$, where γ is the Lorentz factor and $N(\gamma)$ the number density of electrons with energy between γ and $\gamma + d\gamma$ and n_{CR0} normalization constant. Furthermore, we assume that their velocity and pitch angle distribution is isotropic. Both simplifications are consistent with observations and are widely used by many authors (e.g. Sun et al. 2008; Waelkens et al. 2009, as most recent examples). Note that the intrinsic degree of polarization of synchrotron radiation depends on the energy spectral index p and is given by

$$\Pi = \frac{p+1}{p+7/3}. \quad (6)$$

The Stokes Q and U parameters of the polarized Galactic synchrotron emission are given by:

$$j_b^Q = j_b^{PIsyn} \cos 2\Phi, \quad (7)$$

$$j_b^U = j_b^{PIsyn} \sin 2\Phi, \quad (8)$$

where Φ is polarization angle defined with respect to the orientation of the magnetic field.

By integrating j_b^{Isyn} , j_b^Q & j_b^U along some LOS (see Eq. 2) we get the total and polarized Galactic synchrotron emission in terms of the brightness temperature (T_b^{Isyn} , T_b^Q & T_b^U). Note that observed polarized emission and polarization angle Φ_{obs} are given by:

$$T_b^{PI} = \sqrt{(T_b^Q)^2 + (T_b^U)^2}, \quad (9)$$

$$\Phi_{obs} = \frac{1}{2} \arctan \frac{T_b^U}{T_b^Q}. \quad (10)$$

2.2 Free-free emission

Radiation due to (de)acceleration of a charged particle in the electrical field of another is called bremsstrahlung or free-free radiation. The Galactic free-free emission originates from electron-ion encounter in the warm ionized gas. As for the synchrotron emission a detail theory of the free-free radiation can be found in e.g.

Rybicki & Lightman (1986) and Wilson et al. (2009), here we give only the necessary formulae.

The optical depth, τ_{ν}^{ff} , of the warm ionized gas at a given low radio frequency ν is:

$$\tau_{\nu}^{ff} = 3.01 \cdot 10^{-8} g_{ff} \left(\frac{T_e}{[K]} \right)^{-\frac{3}{2}} \left(\frac{\nu}{[MHz]} \right)^{-2} \frac{EM}{[cm^{-6}pc]}, \quad (11)$$

where T_e is temperature of the ionized gas, g_{ff} is the Gaunt factor of the free-free transition given by:

$$g_{ff} = \ln \left[4.95 \cdot 10^{-5} \left(\frac{\nu}{[MHz]} \right)^{-1} \right] + 1.5 \ln \left(\frac{T_e}{[K]} \right), \quad (12)$$

and EM is emission measure defined as:

$$\frac{EM}{[cm^{-6}pc]} = \int n_e^2 ds. \quad (13)$$

The integral is taken over the LOS, where n_e in cm^{-3} is the electron density of the warm ionized gas.

The Galactic free-free emission in terms of brightness temperature, j_b^{ff} , is given by:

$$j_b^{ff} = T_e (1 - e^{-\tau^{ff}}). \quad (14)$$

Note that for optically thin ionized gas, j_b^{ff} is simply given by $j_b^{ff} = T_e \tau^{ff}$.

2.3 Faraday rotation

When the polarization angle of an electromagnetic wave is rotated while passing through a magnetized plasma, the effect is called Faraday rotation (for details see Rybicki & Lightman 1986; Wilson et al. 2009). The rotation depends on the frequency of the wave, ν , electron density, n_e , and magnetic field component parallel to the LOS, B_{\parallel} :

$$\Phi = \Phi_0 + \frac{e^3}{2\pi m_e^2 c^2} \nu^{-2} \int n_e B_{\parallel} ds, \quad (15)$$

where the polarization angle of the wave before rotation is denoted with Φ_0 . Eq. 15 is also written as $\Phi = \Phi_0 + RM\lambda^2$ with λ in units of m and RM (rotation measure) defined as:

$$\frac{RM}{[rad m^{-2}]} = 0.81 \int \frac{n_e}{[cm^{-3}]} \frac{B_{\parallel}}{[\mu G]} \frac{ds}{[pc]}. \quad (16)$$

The RM is positive when B_{\parallel} points towards observer and negative when B_{\parallel} points in away.

3 OBSERVATIONAL CONSTRAINTS

There are several all-sky maps of the total Galactic diffuse radio emission at different frequencies and angular resolutions (Haslam et al. 1982; Reich & Reich 1986, 1988; Page et al. 2007). The 150 MHz map by Landecker & Wielebinski (1970) is the only all-sky map in the frequency range (100 – 200 MHz) relevant for the EoR experiments, but has only 5° resolution.

At high Galactic latitudes the minimum brightness temperature of the Galactic diffuse emission is about 20 K at 325 MHz with variations of the order of 2 per cent on scales from 5 to 30 arcmin across the sky (de Bruyn et al. 1998). At the same Galactic latitudes, the temperature spectral index of the Galactic emission is about -2.55 at between 100 and 200 MHz (Rogers & Bowman 2008) and steepens towards higher frequencies (e.g. Platania

et al. 1998; Bennett et al. 2003; Bernardi et al. 2004). Furthermore, the spectral index gradually changes with position on the sky. This change appears to be caused by a variation in the spectral index along the line of sight. An appropriate standard deviation in the power law index, in the frequency range 100–200 MHz appears to be of the order of ~ 0.1 (Shaver et al. 1999).

Using the obtained values at 325 MHz and assuming the frequency power law dependence, the Galactic diffuse emission is expected to be 140 K at 150 MHz, with ~ 3 K fluctuations.

Studies of the Galactic polarized diffuse emission are done mostly at high radio (~ 1 GHz) frequencies (for a recent review see, Reich 2006). At lower frequencies (~ 350 MHz), there are several fields done with the Westerbork telescope (WSRT) (Wieringa et al. 1993; Haverkorn et al. 2003; Schnitzler 2008). These studies revealed a large number of unusually shaped polarized small-scale structures of the Galactic emission, which have no counterpart in the total intensity. These structures are usually attributed to the Faraday rotation effects along the line of sight.

At high Galactic latitudes, the Galactic polarized emission at 350 MHz is around 5 K or more, on 5–10 arcmin scales (de Bruyn et al. 2006). At 150 MHz this polarized emission would scale to few tens of Kelvin if it were Faraday thin. However, depolarization, that is prominent at low radio frequencies, can significantly lower the level of polarized emission.

Recently, a comprehensive program was initiated by the LOFAR-EoR collaboration to directly measure the properties of the Galactic radio emission in the frequency range relevant for the EoR experiments. The observations were carried out using the Low Frequency Front Ends (LFFE) on the WSRT radio telescope. Three different fields were observed. The first field was a highly polarized region known as the “Fan region” in the 2nd Galactic quadrant at a low Galactic latitude of $\sim 10^\circ$ Bernardi et al. (2009). The second field was a very cold region in the Galactic halo ($l \sim 170^\circ$) around the bright radio quasar 3C196, and third was a region around the North Celestial Pole (NCP, $l \sim 125^\circ$ Bernardi et al. 2010). The last two fields represent possible targets for the LOFAR-EoR observations. Below we present the main results of these papers.

In the “Fan region”, fluctuations of the Galactic diffuse emission were detected at 150 MHz for the first time. The fluctuations were detected both in total and polarized intensity, with an *rms* of 14 K (13 arcmin resolution) and 7.2 K (4 arcmin resolution) respectively (Bernardi et al. 2009). Their spatial structure appeared to have a power law behavior with a slope of -2.2 ± 0.3 in total intensity and -1.65 ± 0.15 in polarized intensity. Note that, due to its strong polarized emission, the “Fan region” is not a representative part of the high Galactic latitude sky.

Fluctuations of the total intensity Galactic diffuse emission in the “3C196” and “NGP” fields were also observed on scales larger than 30 arcmin, with an *rms* of 3.3 K and 5.5 K respectively.

Patchy polarized emission was found in the “3C196” field, with an *rms* value of 0.68 K on scales larger than 30 arcmin (Bernardi et al. 2010). Thus, the Galactic polarized emission fluctuations seem to be smaller than expected by extrapolating from higher frequency observations. Recent observations at mid-galactic latitude with the Giant Metrewave Radio Telescope (GMRT) confirm this conclusion, by setting an upper limit to the diffuse polarized Galactic emission in their field to be < 3 K at 150 MHz and on scales between 36 and 10 arcmin (Pen et al. 2009).

4 SIMULATION

In this section, the various components of the simulation that lead towards the brightness temperature maps of the Galactic synchrotron and free-free emission in a total and polarized intensity are explained. Because the simulated maps will be used as a foreground template for the LOFAR-EoR end-to-end simulations, the foreground simulations assume the angular and frequency range of the LOFAR-EoR experiment, i.e. $10^\circ \times 10^\circ$ maps from 115 MHz to 180 MHz. In addition, all parameters of the simulations can be tuned to any desired value or have any desired characteristic, allowing to explore the parameter space of our Galactic model.

Our algorithm is based on a 3D grid in a Cartesian coordinate system, where xy -plane represents the angular plane of the sky (“flat sky” approximation valid for a small field of view) and z axis is a line of sight direction in parsecs.

The first step in our simulation is to calculate, at a certain frequency, the 3D emission coefficient of the Galactic synchrotron and free-free emission expressed in terms of unit temperature (see Eq. 3 & 14). The emission coefficients are obtained from the cosmic-ray, n_{CR} , and thermal electron, n_e , densities, and the Galactic magnetic field (\vec{B}). Given the 3D emission coefficients, we integrate along the LOS to obtain the brightness temperature maps of the Galactic synchrotron and free-free emission at a certain frequency. The calculation also includes Faraday rotation effects. Note that all parameters of the simulation are set in such a way that simulated maps are quantitatively (e.g. presence of the structures at different scales, spatial and frequency variations of the brightness temperature and its spectral index, etc.) in agreement with the observations overviewed in Sec. 3. A detail description of all input parameters (n_{CR} , n_e and \vec{B}) and the algorithm follow. A few examples of simulated Galactic emission data cubes are presented in Sec. 5, together with a quantitative comparison with the observations.

4.1 Cosmic ray electron density

The cosmic ray (CR) electrons relevant for the Galactic synchrotron emission have energies between 400 MeV and 25 GeV, assuming a Galactic magnetic field of a few μG (Webber et al. 1980). In this energy range, the CR electron distribution can be described as a power law. The power law is normalized according to the measurements obtained in the solar neighborhood. However, the locally measured values might not be a good representative for the CR density elsewhere in the Galaxy (e.g. Strong et al. 2004). As a consequence, the CR electron distribution is weakly constrained.

In our simulation, uniform CR electron density distribution is assumed in the xy -plane. In the z direction we follow Sun et al. (2008) and assume an exponential distribution:

$$n_{\text{CR}} = n_{\text{CR}0} \exp\left(\frac{-z}{1\text{kpc}}\right). \quad (17)$$

Note that $n_{\text{CR}0}$ depends on the assumed energy spectral index p of the CR electrons, so it is normalized according to Eq. 2 for the synchrotron radiation. Assuming $T_b(150\text{ MHz}) \simeq 145\text{ K}$, $B_\perp = 5\ \mu\text{G}$ and $p = 2$, we get $n_{\text{CR}0} \simeq 1.4 \cdot 10^{-8}\text{ cm}^{-3}$.

In the desired frequency range of our simulation, the assumed energy spectral index $p = 2$ is consistent with the values of the typically observed brightness temperature spectral index of the Galactic synchrotron emission ($\beta = -2.5$, see Sec. 3)⁸.

⁸ The brightness temperature spectral index β of the Galactic synchrotron

In addition, the spatial variations of the spectral index p are introduced to mimic the observed spatial fluctuations of β . We follow our previous model (Jelić et al. 2008) and simulate the variation of p (or β) as a Gaussian random field. For the power spectrum of the Gaussian random field it is assumed a power law with index -2.7 (Jelić et al. 2008).

4.2 Galactic magnetic field

The Galactic magnetic field has two components: a regular component \vec{B}_r and a random component \vec{b} , so that the total Galactic magnetic field is given as $\vec{B} = \vec{B}_r + \vec{b}$ (for review see Beck et al. 1996; Han & Wielebinski 2002). The regular component is usually simulated as a combination of a disk and a halo field, whereas the random field component is simulated as a Gaussian random field, Gaussian random field, (for details see Sun et al. 2008; Sun & Reich 2009). Note that for our calculations, we split \vec{B} in a component parallel (B_{\parallel}) and perpendicular (B_{\perp}) to the LOS, so that Faraday rotation is defined by B_{\parallel} and synchrotron emission by B_{\perp} .

Considering the aim of our effort to simulate the Galactic emission for a small patch of the sky, we treat the regular field component in a simplified way. The regular field component is assumed to be uniform in the xy -plane and to have an exponential decrease in the z direction. The typical value of the regular field component is a few μG (for review see Beck et al. 1996; Han & Wielebinski 2002).

For the random field component we follow Sun et al. (2008); Sun & Reich (2009) and simulate it as a Gaussian random field. The power spectrum of the field follows a power law, with spectral index $-8/3$. This spectral index is commonly used for a Kolmogorov-like turbulence spectrum.

In our simulation, the realization of the random field component is done in the following way. First we generate three different Gaussian random fields for the b_x , b_y and b_z component. From those three fields, we then calculate the amplitude of \vec{b} and normalize it to the desired value. A typical value for the mean random field strength is $b = 3 \mu G$ (Sun et al. 2008).

4.3 Thermal electron density

At high Galactic latitudes, the warm ionized medium consists mostly of diffuse ionized gas (DIG) with total emission measure of $\sim 5 \text{ pc cm}^{-6}$ and $T_e = 8000 \text{ K}$ (Reynolds 1990). The properties of the DIG can be traced by its free-free emission and dispersion measure⁹ (DM) of pulsars (e.g. Gaensler et al. 2008).

Recent simulations of the Galactic emission (Sun et al. 2008; Waelkens et al. 2009; Sun & Reich 2009) used the Cordes & Lazio (2002) model for the thermal electron distribution. That model simulates the Galaxy as several large-scale (e.g. thin and thick disk, and spiral arms) and small-scale (e.g. supernovae bubbles) structures. In our simulation, we follow our previous model of the Galactic free-free emission (Jelić et al. 2008) and simulate the thermal electron density distribution as a Gaussian random field with the power law type of the spectrum. The spectral index of the power law is

emission and the energy spectral index p of the CR electrons are related as $\beta = -(p + 3)/2$.

⁹ The dispersion measure is defined as the integral of the thermal electron density along the LOS. Knowing the distance to the pulsars (e.g. determined by parallax), an electron density model can be obtained by a fit to the observed DMs.

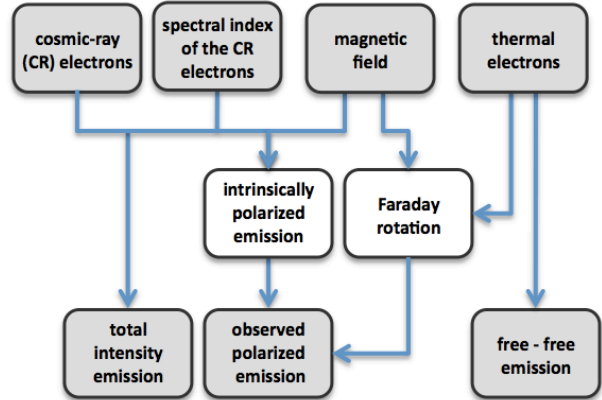


Figure 1. Flow chart of the algorithm: the Galactic emission (synchrotron and free-free) is derived from the physical quantities and 3D characteristics of the Galaxy, i.e. cosmic ray, n_{CR} , and thermal electron, n_e , density; and magnetic field, \vec{B} . In addition, the algorithm includes Faraday rotation effects.

–3. The amplitude of the Gaussian random field (thermal electron density) is normalized in a way to match the typical observed EM of the quasars at high Galactic latitudes (EM values are taken from Berkhuijsen et al. 2006).

It is important to note that our model is flexible to include additional features of the thermal electron distribution, e.g. dense bubbles or clumpy distribution. Some of these features are presented in Sec. 5.

4.4 The Algorithm

Here we summarize the steps we follow to obtain maps of the Galactic emission at a desired frequency. The flow chart of the algorithm is presented in Fig. 1.

(i) The CR electron density, n_{CR} , and the regular component, \vec{B}_r , of the Galactic magnetic field are defined on 3D grid. The distributions of n_{CR} and \vec{B}_r are uniform in the xy -plane and have an exponential decrease in the z direction.

(ii) The spatial distribution of the CR electron energy spectral index, p , the random component, \vec{b} , of the Galactic magnetic field and the thermal electron density, n_e , are simulated as Gaussian random fields. The Gaussian random fields are normalized to result in a desired rms value of the brightness temperature maps. Note that additional features in the electron distribution are added if desired.

(iii) The parallel, B_{\parallel} , and perpendicular, B_{\perp} , component of the total Galactic magnetic field, \vec{B} , are calculated from \vec{B}_r and \vec{b} .

(iv) Using Eq. 3, the emission coefficients of the Galactic total, $j_b^{I\text{syn}}$, and polarized, $j_b^{P\text{syn}}$, synchrotron radiation are calculated.

(v) The optical depth, τ^{ff} , and emission coefficient, j_b^{ff} , of the thermal plasma are obtained from Eq. 11 & 14. Note that these effects are really significant only on the lowest radio frequencies.

(vi) Absorption of the synchrotron emission by the optical thickness of the ionized plasma is taken into account as $\exp(-\tau^{ff})$ factor.

(vii) Using Eq. 15, the Faraday rotation effect is calculated and the polarization angle, Φ , is obtained. Note that the intrinsic polarization angle, Φ_0 , is defined as the inclination of B_{\perp} .

(viii) The Stokes Q and U emission coefficients of the polarized emission, j_b^Q & j_b^U , are calculated using Eq. 7 & 8.

(ix) By integrating $j_b^{I\text{syn}}$, j_b^Q & j_b^U along some LOS (see Eq. 2),

the total and polarized Galactic synchrotron emission in terms of the brightness temperature, $T_b^{I_{syn}}$, T_b^Q & T_b^U , are obtained.

(x) Finally, the maps of the total polarized emission (T_b^{PI}) and observed polarization angle Φ_{obs} is calculated using Eq. 9 & 10.

In the following section we will show some examples of the Galactic emission maps obtained by this algorithm.

5 EXAMPLES OF SIMULATED GALACTIC EMISSION

Here we demonstrate the ability of our algorithm to realistically simulate Galactic synchrotron and free-free emission both in total and polarized intensity. We also quantitatively compare results of our simulations with the observations.

5.1 Simulated data cubes

The simulated data cubes are presented for four cases of the Galactic emission. First three models show ability of our algorithm to simulate different cases of Faraday rotation and depolarization, while the last model is tailored to be in agreement with Bernardi et al. (2009) observations of the Fan region.

- **Model A:** CR electrons are distributed in a region of 1 kpc in depth along the LOS ($n_{CR0} = 1.4 \times 10^{-8} \text{ cm}^{-3}$). In front of this region, there is a thermal electron cloud of 300 pc in depth along the LOS, with an average emission measure of $\overline{EM} = 8 \text{ cm}^{-6} \text{ pc}$, and $T_e = 8000 \text{ K}$. The thermal electron cloud is acting as a “Faraday screen” that rotates the polarization angle of synchrotron emission. It is assumed that Galactic magnetic field is uniform throughout the region ($B_{r,\parallel} = 3 \mu\text{G}$ and $B_{r,\perp} = 2.5 \mu\text{G}$).

- **Model B:** Both CR and thermal electrons are mixed in the region of 1 kpc in depth along the LOS (n_{CR0} , \overline{EM} , T_e and \vec{B}_r are the same as in model A). The polarized synchrotron radiation is differentially Faraday rotated. Since the Galactic magnetic field has the same characteristics as in model A, depolarization is produced only by thermal plasma.

- **Model C:** The same as model B, but in the middle of the simulated region there is a dense thermal electron bubble 300 pc in depth along the LOS, with a strong magnetic field ($B_{\parallel} = 10 \mu\text{G}$). The Faraday rotation along the bubble will be much larger than in other parts of the region. Note that the size of the bubble is quite large in order to make its appearance in the final maps more clear. Moreover, it is assumed that Galactic magnetic field is not uniform throughout the region: $B_{r,\parallel}$ exponentially decreases along the LOS. We also include a random magnetic field component as a Gaussian random field ($b_{\parallel} = 3 \mu\text{G}$, see Sec. 4). Depolarization is then produced both by thermal plasma and variations of the magnetic field.

- **Model D:** This model is based on a proposed cartoon of the magnetized interstellar medium in the Fan region by Bernardi et al. (2009, see fig. 12). The intrinsically polarized background emission passes through multiple Faraday screens which make the spatial distribution of the polarized emission more clumpy. A bubble of ionized thermal plasma sits between the Faraday screens and the observer. This bubble further rotates the polarized emission to the higher values of RM. All parameters of this model are set to match the observed properties of this region: fluctuations of the diffuse emission at 150 MHz and their power-law type of the power spectrum (see Bernardi et al. 2009, and Sec. 3).

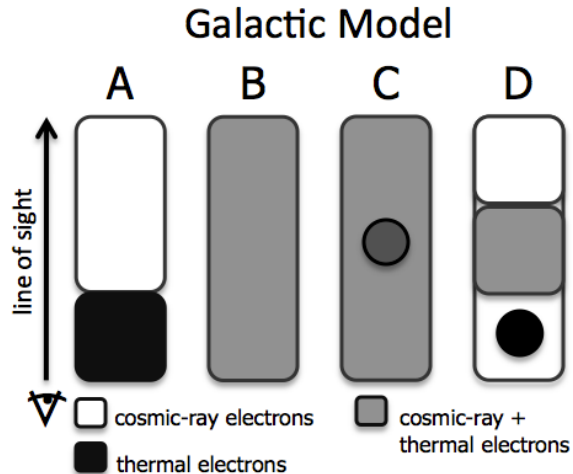


Figure 2. The intensity distributions (see Fig. 3 & 4) are obtained for four different models of the Galactic emission. The first (model A) assumes that synchrotron and free-free emitters are spatially separated, so that thermal plasma acts as a “Faraday screen”. The second, third and fourth (model B, C, & D) have regions where both types permeate in a different way. The synchrotron emission is differentially Faraday rotated and depolarization occurs.

Cartoons of these four models are given in Fig. 2. The Galactic emission maps are obtained in the frequency range from 115 to 180 MHz, with 0.5 MHz step.

In the first three models the synchrotron emission originates from the same CR electron distribution with uniform B_{\perp} component of the Galactic magnetic field. Therefore, the brightness temperature maps of the total and intrinsic¹⁰ polarized synchrotron emission are equivalent in all three models. The same is valid for the free-free emission, i.e., n_e is normalized to the same value of EM . The resulting $10^{\circ} \times 10^{\circ}$ maps at 150 MHz are shown in Fig. 3.a, b & d, while the *mean* and *rms* of the maps are given in Table 1. A map of the brightness temperature spectral index β of simulated total intensity synchrotron emission is shown in Fig. 3.c.

Simulated polarized emission maps of the first three Galactic synchrotron emission models are shown in Fig. 4.a, b & c. Their *mean* and *rms* values together with the degree of polarization and depolarization are listed in Table 1. A random line through synchrotron total and polarized intensity frequency data cubes of first three models are given in Fig. 6.

Simulated total and polarized emission images of the Fan region (model D) are given at 150 MHz in Fig. 5 a & b. For easier comparison with the observation an RM image, obtained by applying rotation measure synthesis technique (Brentjens & de Bruyn 2005) on the simulated data, is shown in Fig. 5 c.

5.2 Discussion and tests of the algorithm

First test of the algorithm is to estimate the degree of intrinsic polarization, Π , of the simulated map (Fig. 3.b). By dividing the intrinsic polarized emission map and the total intensity map, we

¹⁰ Here, the intrinsic polarized emission, iPI_{syn} , means emission defined by Eq. 3. Note that the polarization angle of this emission is assumed to be uniform across the whole region. Thus any effect caused by thermal electrons or B_{\parallel} will be immediately apparent.

obtain $\Pi = 0.69$ (see Table 1). This value is in a good agreement with the expected theoretical value $\Pi_{p=2} = 9/13$ (see Eq. 6).

Further we explore morphological characteristics of the simulated polarized emission by comparing the image of intrinsically polarized emission (Fig. 3.b) with the images of polarized emission of the first three models (see Fig. 4). Note that degree of polarized and depolarized emission is given in Table 1.

Model A assumes that there is no region in which the plasma (thermal electron cloud) is mixed with CR electrons. Therefore, polarization angle of synchrotron emission along the LOS are Faraday rotated by an equal amount (defined by Eq. 15). Since there is no differential Faraday rotation, depolarization does not occur and the polarized intensity of the synchrotron emission is unchanged (see Fig. 4.a and Table 1). Morphology of the polarization angles over the map is determined only by the spatial RM variations of the plasma.

In order to test the above results, we correlate a polarized emission image with a total intensity, and polarization angles with the image of free-free emission. The cross correlation coefficient¹¹ is $C = 1$ in both cases. Since the polarized emission is completely correlated with the total intensity, and the free-free emission, which traces thermal plasma, with polarization angles, we conclude that our algorithm is performing as expected. The spatial structures of polarized emission are unchanged, while the structures of polarization angle follow thermal plasma.

In B and C models there are regions where both CR and thermal electrons are mixed. In those regions the polarization angle of the synchrotron radiation is then differentially Faraday rotated along the LOS. As a result, the polarized synchrotron radiation is quenched and the level of the polarized emission is weaker than intrinsic polarization emission (see Table 1). In addition to depolarization produced by the mixed regions, in model C depolarization is also produced by variations of the Galactic magnetic field along the LOS.

As for model A, we calculate correlations between the total and polarized images. In both models (B & C) we find much weaker correlation ($C_{B,C} = 0.3, 0.1$) than in model A. The weaker correlation results from differential Faraday rotation along the LOS, which changes the morphology of polarized emission both in intensity and angle. To illustrate this we correlate the polarized synchrotron emission with the free-free emission. We find anti-correlation in both models ($C_{B,C} = -0.7, -0.5$). The intensity of the polarized emission is more quenched in the regions that show stronger free-free emission (regions of denser plasma). Moreover, model C shows weaker (anti)correlations than model B, due to Faraday structures produced by magnetic field.

The last aspect of the algorithm, which needs to be verified, is the frequency behavior of the simulated Galactic emission. It is expected that the synchrotron emission shows roughly a power law along the frequency (see Eq. 3). By examining Fig. 6, one can see that simulated synchrotron emission indeed shows a power law behavior in total intensity. However, in polarized intensity only model A shows a power law behavior. All the other models show charac-

¹¹ The cross correlation coefficient between two images ($a_{i,j}$ and $b_{i,j}$) with the same total number of pixels n is defined as:

$$C_0 = \frac{1}{n-1} \sum_{i,j} \frac{(a_{i,j} - \bar{a})(b_{i,j} - \bar{b})}{\sigma_a \sigma_b}, \quad (18)$$

where \bar{a} (\bar{b}) is the mean and σ_a (σ_b) the standard deviation of the image a (b).

Table 1. The *mean* and *rms* value of the maps shown in the Fig. 3 & 4. All the values are given in kelvin. For completeness, degree of polarized (PI/T) and depolarized (*dep.*) emission is calculated.

	I_{syn}	I_{ff}	iPI_{syn}	PI_A	PI_B	PI_C
mean	142	1.5	98	98	10	11
rms	3	0.1	2	2	5	5
PI/I	-	-	69%	69%	7%	8%
<i>dep.</i>	-	-	0%	0%	90%	88%

teristic fluctuations caused by differential Faraday rotation (Burn 1966). Note that fluctuations show richer structures, as in model C, if the differential Faraday rotation is more prominent.

The calculated brightness temperature spectral index, β_{syn} , variations of the simulated Galactic synchrotron emission are given in the Fig. 3.c. The variations of β_{syn} are estimated by fitting the data with a linear functions along the frequency in logarithmic scale. The *mean* value of β_{syn} is -2.50 , which is in a good agreement with the expected theoretical value $\beta_{p=2} = -(p+3)/2 = -2.55$. A slight difference between the two is caused by the 3D spatial variations of the spectral index p .

Based on discussion and tests of the algorithm presented in this subsection, we can conclude that our algorithm is simulating Galactic emission as expected. In the following subsection, we will compare the simulated data cubes with the observations.

5.3 Comparison with observations

Input parameters of the simulation (properties of the CR electrons, thermal electrons, and Galactic magnetic field, see subsections 4.1, 4.2 & 4.3) are chosen in such way that the global properties (boundary conditions) of the simulated maps, e.g. morphology and frequency behavior of the Galactic emission, are in agreement with the observations overviewed in Sec. 3:

- the mean value of the simulated synchrotron emission in total intensity, $I_{syn} = 142$ K (see Table 1) is comparable to observed emission at 150 MHz (in the cold regions of the Galaxy at the high galactic latitudes, Landecker & Wielebinski 1970) or to the values obtained by extrapolation from the higher frequencies, i.e., ~ 150 K;
- the mean and variations of the brightness temperature spectral index of the simulated maps, $\beta_{syn} = -2.50$ (see Subsection 5.2) and $\sigma = 0.1$, are in agreement with the observed values, $\beta_{syn}^{obs} = -2.55$ and $\sigma_{syn}^{obs} \approx 0.1$ (e.g. Rogers & Bowman 2008, and references therein);
- the spatial structures of the simulated Galactic emission in total intensity are morphologically similar to the observed emission around 150 MHz (Bernardi et al. 2009, 2010) and $\sim 300 - 400$ MHz (e.g. Haslam et al. 1982; de Bruyn et al. 1998, and references in Sec. 3), i.e., power law type of the power spectrum with a negative power law index (more power on the large scales);
- the simulated polarized emission (e.g. model B, C & D) shows small-scale structures, which have no counter parts in the total intensity, e.g. like a number of observations with the WSRT (see Sec. 3);
- the simulated distribution of the thermal electrons reproduce the typical observed $EM \sim 10 \text{ cm}^{-6} \text{ pc}$ at the high Galactic latitudes (Berkhuijsen et al. 2006).
- the simulated Galactic emission (see Fig. 6) shows characteristic power law behavior along the frequency in total intensity,

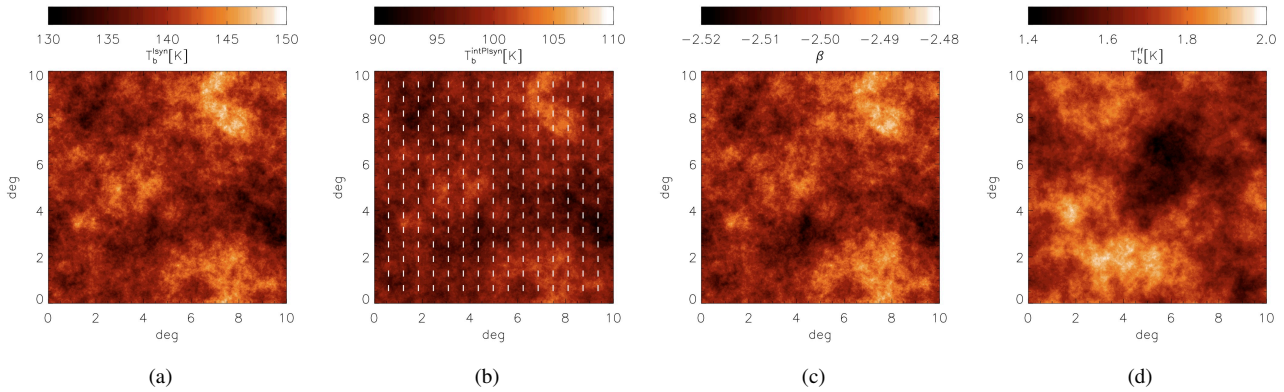


Figure 3. Simulated maps of the total (Fig. 3.a) and intrinsic polarized (Fig. 3.b) intensity of the Galactic synchrotron emission. The polarization angle is plotted over the polarized map as a white lines. The map of brightness temperature spectral index β of simulated total intensity synchrotron emission is shown in Fig. 3.c. The total intensity map of the free-free emission is shown in Fig. 3.d. The angular size of the maps are $10^\circ \times 10^\circ$, with ~ 1 arcmin resolution. The color bar represents the brightness temperature T_b of emission in kelvin at 150 MHz. The *mean* and *rms* value of the maps are given in the Table 1.

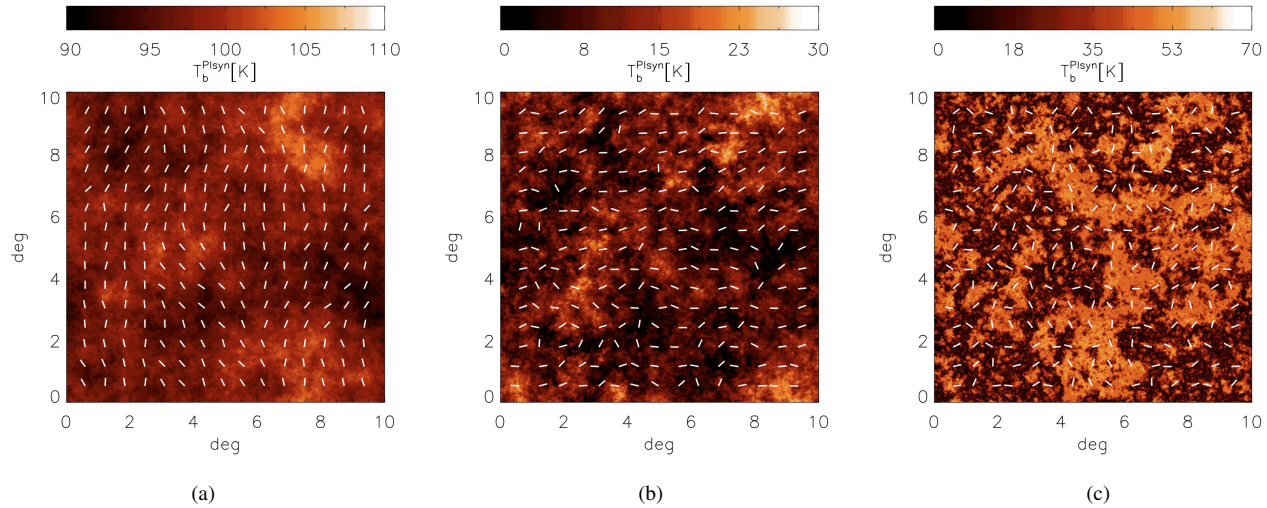


Figure 4. Simulated maps of the polarized intensity and polarization angle (white lines) of the four different Galactic synchrotron emission models (A, B and C from left to right). The angular size of the maps are $10^\circ \times 10^\circ$, with ~ 1 arcmin resolution. The *mean* and *rms* values of the maps at 150 MHz are given in the Table 1.

while in polarized intensity can reproduce the characteristic polarization functions (Burn 1966).

We also quantitatively compare the simulated emission in the Fan region (our model D) with the observations of this region at 150 MHz (Bernardi et al. 2009):

- simulated fluctuations have an rms of 14 K in total intensity and rms of 7 K in polarized intensity (these values are the same as the observed ones);
- the power law indices of the power spectrum obtained from the simulation are in agreement with the observations: -2.2 in total intensity, and -1.6 in polarized intensity;
- simulated maps (see Fig. 5) show similar morphological structures (their statistical distribution of power) as the observed ones (fig 5., 8. & 10. in Bernardi et al. 2009);
- a simulated rotation measure cube¹² shows similar morpho-

logical structures as the observed ones, i.e., at -2 rad m^{-2} there is a hole in the emission, a bubble with a diameter of $\sim 2^\circ$.

Here we emphasize that we have also successfully tested our algorithm at the higher frequencies (~ 350 MHz) by simulating Galactic emission towards the cluster Abel 2255. The simulated maps have been compared with the observations obtained by R.F. Pizzo et al. (*in prep.*, *private communication*). Details of these simulations will be presented in a separate paper (Jelić et al., *in prep.*).

To summarize, simulated maps show all observed characteristics of the Galactic emission, e.g. presence of the structures at different scales, spatial and frequency variations of the brightness temperature and its spectral index, complex Faraday structures, and depolarization. Based on these results, we conclude that our model is able to simulate realistic maps of the Galactic emission both in total and polarized intensity, and can be used as an realistic foreground model in simulations of the EoR experiments.

¹² The rotation measure cube is obtained using the rotation measure synthesis method (Brentjens & de Bruyn 2005).

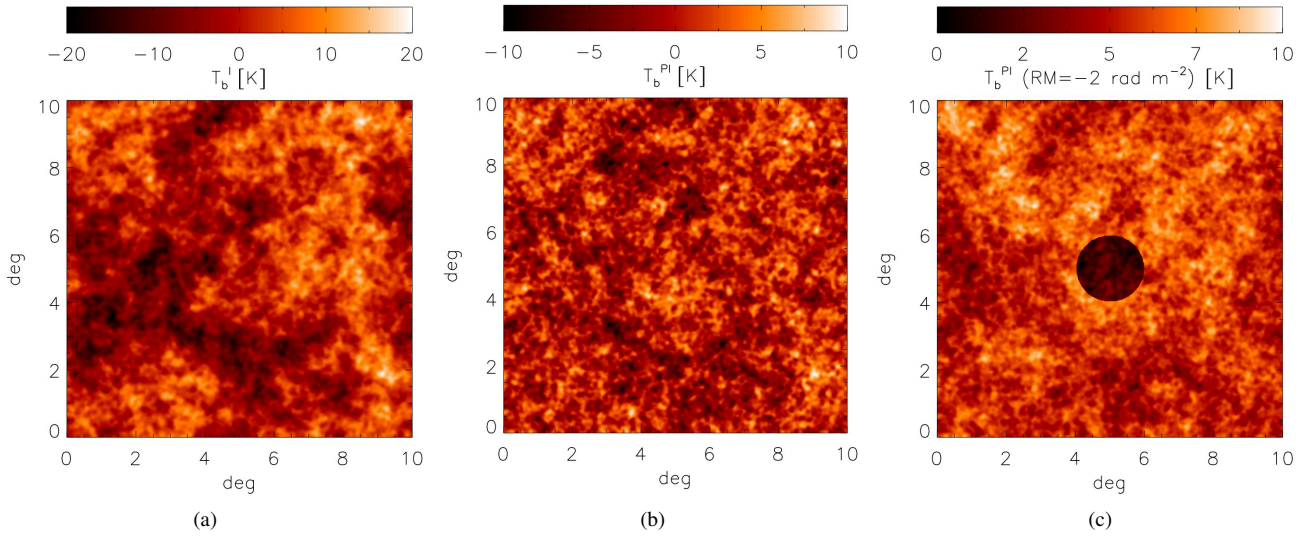


Figure 5. Simulated maps of the Fan region (model D) in total (Fig. 5 a) and polarized intensity (Fig. 5 b). An RM image obtained by applying rotation measure synthesis technique on the simulated data is shown in Fig. 5 c.

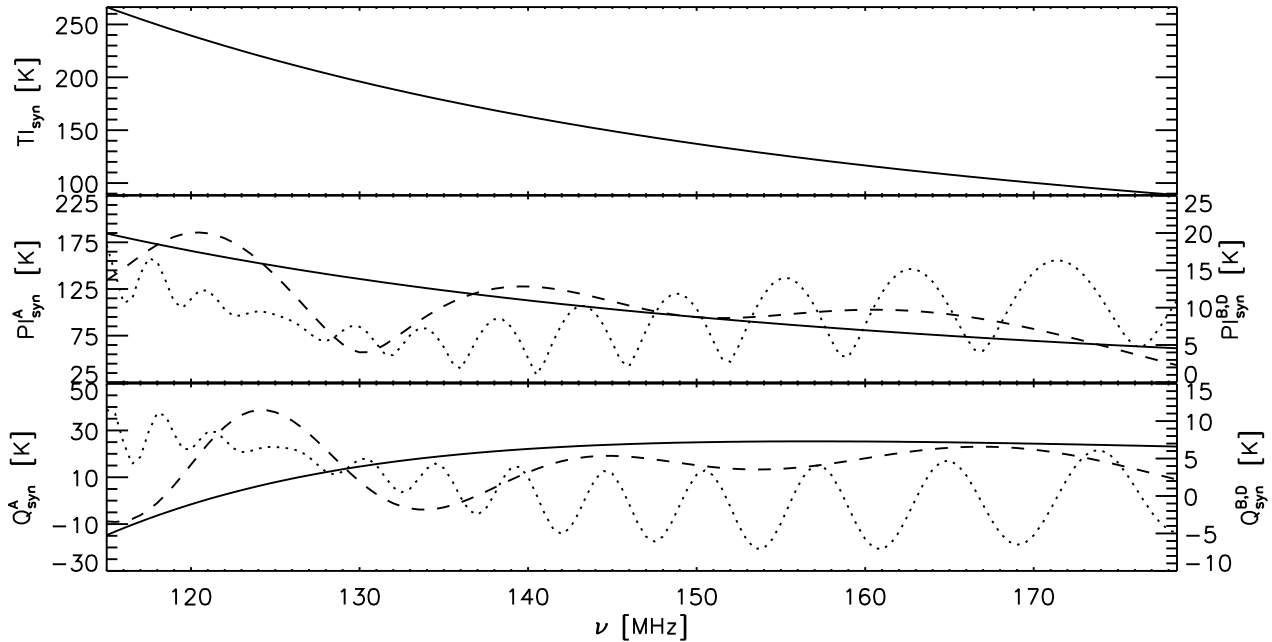


Figure 6. A random line through synchrotron total intensity (TI_{syn}) and polarized intensity (PI_{syn}, Q_{syn}) frequency data cubes. The *solid lines* are for the Galactic MODEL A, *dashed lines* for MODEL B and *dotted lines* for MODEL D. TI_{syn} is the same in all four models, while U_{syn} is not presented since it is similar to Q_{syn} . Note the polarized structures along the frequency direction. An improper polarization calibration of the instrument could cause a leakage of these structures to the total intensity and severely contaminate the EoR signal.

6 LOFAR-EOR SIMULATION PIPELINE

The LOFAR-EoR project relies on a detailed understanding of astrophysical and non-astrophysical contaminations that can contaminate the EoR signal: the Galactic and extragalactic foregrounds, ionosphere, instrumental effects and systematics. In order to study these components and their influence on the detection of the EoR signal, a LOFAR-EoR simulation pipeline is being developed by the LOFAR-EoR team. The pipeline consists of the three main modules: the EoR signal (based on simulations described in Thomas et al. 2009), the foregrounds (based on this paper and Jelić

et al. 2008) and the instrumental response (described on Labropoulos et al. 2009).

In this paper we use the LOFAR-EoR pipeline to illustrate the need for excellent calibration of the instrument in order to reliably detect the EoR signal (see Sec. 7). The following two subsections present a brief overview of the EoR signal and instrumental response modules.

6.1 EoR signal

The predicted differential brightness temperature of the cosmological 21 cm signal with the CMB as the background is given by (Field 1958, 1959; Ciardi & Madau 2003):

$$\delta T_b = 26 \text{ mK } x_{\text{HI}}(1 + \delta) \left(1 - \frac{T_{\text{CMB}}}{T_s}\right) \left(\frac{\Omega_b h^2}{0.02}\right) \left[\left(\frac{1+z}{10}\right) \left(\frac{0.3}{\Omega_m}\right)\right]^{1/2}. \quad (19)$$

Here T_s is the spin temperature, x_{HI} is the neutral hydrogen fraction, δ is the matter density contrast and $h = H_0/(100 \text{ km s}^{-1} \text{ Mpc}^{-1})$. Throughout we assume Λ CDM-cosmology with WMAP3 parameters (Spergel et al. 2007): $h = 0.73$, $\Omega_b = 0.0418$, $\Omega_m = 0.238$ and $\Omega_\Lambda = 0.762$. In addition we assume that $T_s \gg T_{\text{CMB}}$, which is assumed in most of the current simulations.

The cosmological 21 cm maps (δT_b) are simulated using the BEARS algorithm (Thomas et al. 2009). BEARS is a fast algorithm to simulate the underlying cosmological 21 cm signal from the EoR. It is implemented using an N-body/SPH simulation in conjunction with a 1-D radiative transfer code under the assumption of spherical symmetry of the ionized bubbles. The basic steps of the algorithm are as follows: first, a catalogue of 1D ionization profiles of all atomic hydrogen and helium species and the temperature profile that surround the source is calculated for different types of ionizing sources with varying masses, luminosities at different redshifts. Subsequently, photon rates emanating from dark matter haloes, identified in the N-body simulation, are calculated semi-analytically. Finally, given the spectrum, luminosity and the density around the source, a spherical ionization bubble is embedded around the source, whose radial profile is selected from the catalogue as generated above. For more details we refer to Thomas et al. (2009).

For the purpose of this paper we use the δT_b data cube (2D slices along the frequency/redshift direction) of the cosmological 21 cm signal for the ‘Stars’ patchy reionization model (see Thomas et al. 2009). The data cube consists of 850 slices in the frequency range from 115 MHz to 200 MHz with 0.1 MHz step (corresponding to redshift between 6 and 11.5). Slices have a size of 100 h^{-1} comoving Mpc and are defined on a 512^2 grid. An example of a random line of sight through simulated 21 cm data cube, with angular and frequency resolution matching that of LOFAR, is shown in Fig. 7.

6.2 Instrumental response

In order to produce the dirty maps of the diffuse emission, we calculate the 2D Fourier transform of the data for each correlation on a fine grid of 1.2 arcmin. We assume that there are 24 stations in the LOFAR array that are used for the observations. We then use a bilinear interpolation to estimate the values of the visibilities at the uvw points that correspond to the points sampled by the interferometer pairs of the core. This is done for 4hrs of synthesis, 10 sec integration and for the whole frequency range between 115 MHz and 180 MHz, using a step of 0.5 MHz. The above procedure is implemented as a parallel algorithm in the CHOPCHOP pipeline (see Labropoulos et al, *submitted*). In order to sample the large structure of the foregrounds at scales between 5 and 10 degrees we need interferometer spacing between 6.5 and 13 meters. Thus the PSF acts as a high-pass spatial filter.

Figure 8 shows ‘dirty’ maps of the simulated Galactic synchrotron emission (MODEL B) observed with the core stations of the LOFAR telescope at 138 MHz. The total and polarized intensity maps are shown in Fig. 8.a & b, while the polarization angle is presented in Fig. 8.c. Note that the large scale structures of the emission are missing as the smallest baseline length is approximately 50 m.

7 CONSEQUENCES FOR 21-CM REIONIZATION DETECTION EXPERIMENTS

One of the major challenges of the EoR experiments is the extraction of the EoR signal from the astrophysical foregrounds. The extraction is usually formed in total intensity along the frequency direction due to the following characteristics:

- (i) the cosmological 21 cm signal is essentially unpolarized and fluctuates along the frequency direction (see Fig. 7)
- (ii) the foregrounds are smooth along the frequency direction in total intensity and should only show fluctuations in polarized intensity (see Fig. 6, an example of the Galactic emission that is a dominant foreground component).

Thus, the fluctuating EoR signal can be extracted from the foregrounds by fitting the smooth component of the foregrounds out (e.g. see fig. 12 in Jelić et al. 2008).

All current EoR radio interferometric arrays have an instrumentally polarized response, which needs to be calibrated. If the calibration is imperfect, some part of the polarized signal is transferred into a total intensity and vice versa (hereafter ‘leakages’). As a result, the extraction of the EoR signal is more demanding.

Moreover, the polarized signal could have similar frequency fluctuations as the cosmological signal and as such could possibly severely contaminate it. Thus, to reliably detect the cosmological signal it is essential to minimize the ‘leakages’ and to observe in the regions with the weak polarized foreground emission. We illustrate this through an example for the LOFAR telescope, but the problem is common to all current and planned EoR radio arrays.

7.1 Levels of ‘leakage’

The ‘leakages’ of the total and polarized signal are produced by two effects: the geometry of the LOFAR array and the cross-talk between the two dipoles in one LOFAR antenna. The cross-talk, a leakage in the electronics that can cause the power from one dipole to be detected with other, is small compared to the geometric effects (Labropoulos et al, *submitted*) and we will ignore it for the purpose of this paper.

The geometry of the LOFAR telescope is such that the array antennae are fixed to the ground. Therefore, the sources are tracked only by beam-forming and not by steering the antennae mechanically towards the desired direction. This implies that, depending on the position of the source on the sky, a non-orthogonal (except at the zenith) projection of the two orthogonal dipoles is visible by the source. This projection further changes as the source is tracked over time. Thus, the observed Stokes brightness of the source, \mathbf{S}_{obs} , is given by (Carozzi & Woan 2009):

$$\mathbf{S}_{\text{obs}} = \mathbf{M}\mathbf{S}, \quad (20)$$

where \mathbf{M} is a Mueller matrix that quantifies the distortions of a true source brightness $\mathbf{S} = (I, Q, U, V)$ based on above geometry-projection effect. The Mueller matrix is defined as:

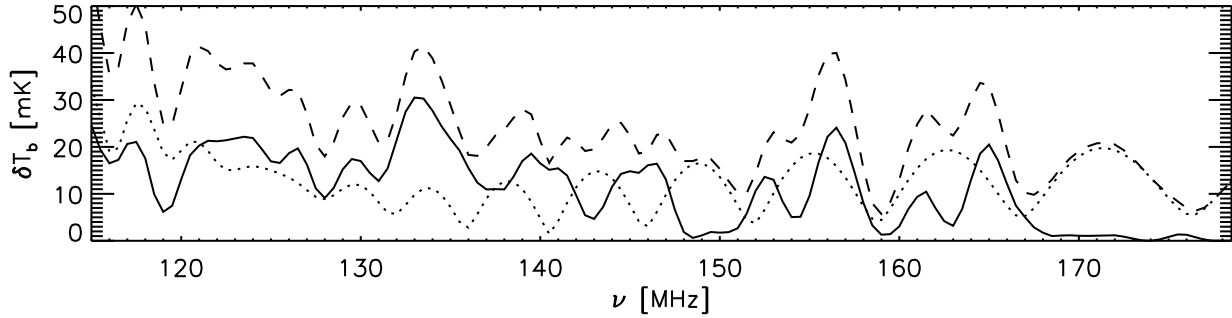


Figure 7. A random line of sight through a simulated 21 cm data cube for the ‘Stars’ patchy reionization history model (solid line). Dotted line shows the ‘leakage’ of the polarized Galactic emission to the total intensity and dashed line is a sum of the two. We assume 0.15% residual ‘leakage’ and we use model D as an example of the Galactic emission. The angular and frequency resolution of the data match that of the LOFAR telescope.

$$\mathbf{M} = \begin{pmatrix} \frac{1}{2}(1+n^2) & -\frac{m^2}{2} + \frac{(1+m^2)l^2}{2(1-m^2)} & -\frac{lmn}{1-m^2} & 0 \\ \frac{1}{2}(l^2-m^2) & 1 - \frac{m^2}{2} - \frac{(1+m^2)l^2}{2(1-m^2)} & \frac{lmn}{1-m^2} & 0 \\ -lm & -lm & n & 0 \\ 0 & 0 & 0 & n \end{pmatrix} \quad (21)$$

with the assumption of a coplanar array. Note that (l, m, n) are direction cosines and that the level of geometry-projection ‘leakage’ therefore varies across the map.

The calculated leakages, for the LOFAR telescope observing at 138 MHz a $5^\circ \times 5^\circ$ patch of the sky around the zenith, vary between 0.1% – 0.7% across the image. For the sky model we use the total and polarized intensity maps of Galactic emission (model C). Further, an instant imaging is assumed, i.e. the sky is not tracked over time. Note that the leakages are tiny around the center of the image, but they increase towards the edges.

The same calculation we repeat for an patch of a sky at 45° altitude. The leakages are now much larger, e.g. for the center of the image the leakage to the total intensity is around 2%, but can reach 20% towards the edges of the image.

Once the tracking of the sources is taken into account, the leakages become even more significant towards the horizon and on the axes parallel to the dipoles, i.e. varying between 0.1%–100% across the sky (for details we refer to Labropoulos et al, *submitted*).

However to be as realistic as possible, we need to take into account that for calibration of the instrument one can use a model of the beam. Using the beam model, one can correct for the polarized instrumental response and decrease the level of ‘leakages’. Thus, in further discussion we refer only to the residual ‘leakages’. Note that for the purpose of this paper we assume that the residual ‘leakages’ are 1%–5% over the whole field of view.

7.2 ‘Leakage’ of the polarized foreground

Here we would like to point out that the residual ‘leakages’ caused by the geometry-projection effect are significant in terms of EoR signal detection. If these ‘leakages’ are not taken properly into account during the calibration of the instrument, the polarized Galactic emission could creep into total intensity signal and severely contaminate the EoR signal. This is illustrated in the Fig. 7.

Figure 7 shows a random line of sight through a simulated 21 cm data cube for the ‘Stars’ patchy reionization history model (solid line). As noted before, the EoR signal shows fluctuations in total intensity. Dotted line shows the ‘leakage’ of the polarized

Galactic emission in the total intensity and dashed line is a sum of the two.

Since we have chosen the Galactic emission model with the differential Faraday rotation (model C), the ‘leakage’ of the Galactic emission shows structures along the frequency direction similar to the EoR signal. Note that the Galactic polarized emission is assumed to be ~ 1 K (in this case our model C), while the level of the residual ‘leakage’ is assumed to be 1.5%. The ‘leaked’ Galactic polarized emission is then of the same order as the EoR signal (~ 15 mK).

In other words, the right combination of the Galactic polarized emission and an inaccurate calibration can result in structures in total intensity that have similar characteristics of the EoR signal. Without knowing the exact characteristics of the Galactic polarized emission in that region it would be impossible to extract the EoR signal. Therefore, the observational windows for the EoR experiments need be in regions of the Galaxy that have very weak or no polarization. Assuming the same residual ‘leakage’ of 1.5%, the Galactic polarized emission should not be stronger than ~ 0.1 K. The ‘leaked’ foreground contamination would then be at least an order of magnitude lower than the EoR signal, which is acceptable for the EoR detection.

However, note that this upper limit on the polarized contamination highly depends on morphology of the Galactic emission. For example, if the Galactic polarized emission does not show structures along the frequency direction (like in our model A), then any ‘leaked’ contamination can be fitted out in the same way as the foregrounds in total intensity. Moreover, if the Galactic polarized emission shows significant structures on scales smaller than resolution of the array, beam depolarization will lower the level of the observed polarized foregrounds and therefore lower the ‘leaked’ contamination as well.

Other possible ways of eliminating a ‘leaked’ polarized foreground from the data are: (i) identifying the polarized emission in rotation measure space using a Faraday rotation measure synthesis (Brentjens & de Bruyn 2005); (ii) using polarization surveys obtained by a different radio telescope and with angular resolution that is preferably higher than the one of the EoR experiments; and (iii) observing the EoR in a multiple regions of the sky.

Note that if someone uses a different polarization data as an EoR foreground template, an instrumental beam depolarization should be take into account. At the same time the advantage is that radio telescopes, which are used for the polarization surveys, suffer from a different systematics (including ‘leakages’) and therefore

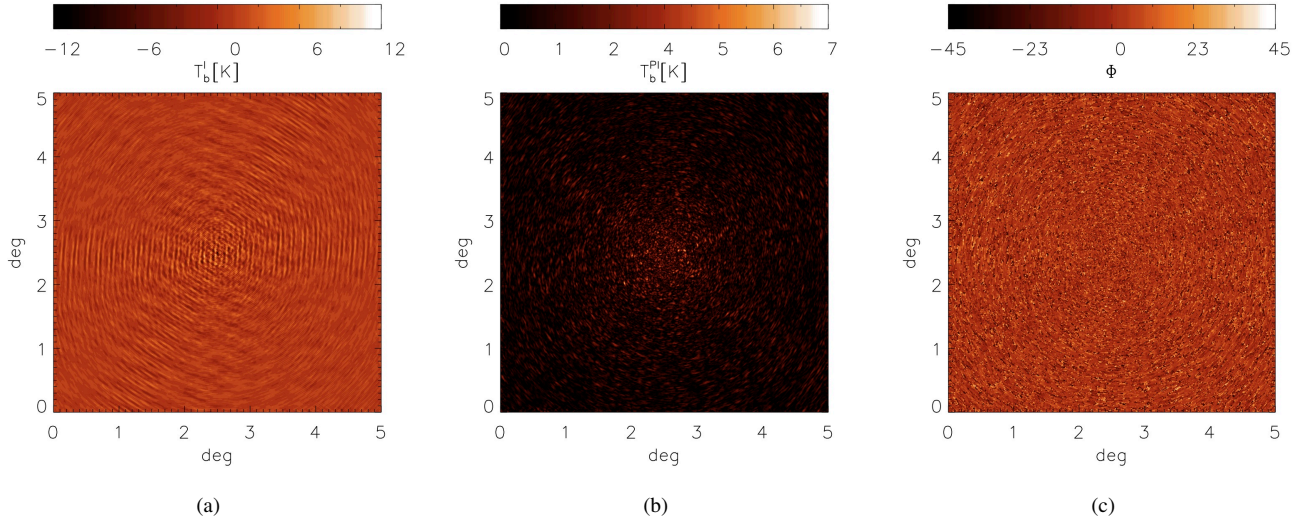


Figure 8. ‘Dirty’ maps of the simulated Galactic synchrotron emission (MODEL B) observed with the core stations of the LOFAR telescope. The total and polarized intensity maps are shown in Fig. 8.a and Fig. 8.b, while the polarization angle is presented in Fig. 8.c. The images are simulated at 138 MHz

comparison of the data observed with a different radio telescopes helps in analysis.

The observations of the EoR signal in multiple windows have advantage of allowing us to cross-correlate the data and increase the significance of the EoR detection. Since the Galactic emission varies across the sky, each observational window will have its own characteristic foreground emission and ‘leakages’. Residuals after foreground removal should not correlate between different observational windows, while the EoR properties should be similar.

8 SUMMARY AND CONCLUSIONS

This paper presents Galactic foreground simulations used as templates for the LOFAR-EoR testing pipeline. The simulations provide maps of the Galactic free-free emission and the Galactic synchrotron emission both in total and polarized intensity. The maps are $10^\circ \times 10^\circ$ in size, with ~ 1 arcmin resolution and cover the frequency range between 115 and 180 MHz pertaining to the LOFAR-EoR experiment. The code however is flexible as can provide simulation over any scale with any spatial and frequency resolution.

The Galactic emission is calculated from a 3D distribution of cosmic ray and thermal electrons, and the Galactic magnetic field. The model assumes two magnetic field components: regular and random. The latter magnetic field and the thermal electron density are simulated as Gaussian random fields with power law power spectra. In addition, the spatial variations of the energy spectral index p of the cosmic ray electrons are introduced to mimic the observed fluctuations of the brightness temperature spectral index β . Note that all parameters of the simulation can be tuned to any desired value and this allows to explore the whole parameter space.

The total and polarized Galactic maps are obtained for four different models of Galactic emission (see Fig. 3 & 4). The first assumes that synchrotron and free-free emitters are spatially separated, such that thermal plasma acts as a ‘Faraday screen’. The amplitude of the polarized emission is unchanged, while the polarization angles Faraday rotate. Other three simulation have regions where both types of emitters are mixed in different ways. The syn-

chrotron emission is differentially Faraday rotated and depolarization occurs (see Table 1).

The main result of our simulations is that we are able to produce realistic Galactic polarized emission that is comparable to observations, i.e., presence of the structures at different scales, spatial and frequency variations of the brightness temperature and its spectral index, complex Faraday structures, and depolarization. The importance of this result comes from the fact that the planned EoR radio arrays have a polarized response and the extraction of the EoR signal from the foregrounds is usually performed along the frequency direction. The Galactic foreground is a smooth function of frequency in a total intensity and it can show fluctuations in polarized intensity. The EoR signal is expected to be unpolarized and to show fluctuations along the frequency direction. Therefore, an imperfect calibration of the instrumental polarized response can transfer a fraction of the polarized signal into a total intensity. As a result, the leaked polarized emission can mimic the cosmological signal and make its extraction almost impossible (see Fig. 7).

Based on our simulations, we conclude that the EoR observational windows need to be in regions with a very low polarized foreground emission, in order to minimize ‘leaked’ foregrounds. Faraday rotation measure synthesis, polarization surveys obtained by different radio telescopes, and a multiple EoR observations will help in mitigating the polarization leakages. However, further simulations and observations are necessary to pin point the best strategy for the EoR detection.

ACKNOWLEDGEMENT

We acknowledge discussion with the LOFAR-EoR key project members. We are also thankful to the anonymous referee for his illustrative and constructive comments. As LOFAR members authors are partly funded by the European Union, European Regional Development Fund, and by ‘Samenwerkingsverband Noord-Nederland’, EZ/KOMPAS.

REFERENCES

- Ali S. S., Bharadwaj S., Chengalur J. N., 2008, *MNRAS*, 385, 2166
- Beck R., Brandenburg A., Moss D., Shukurov A., Sokoloff D., 1996, *ARA&A*, 34, 155
- Bennett C. L., Hill R. S., Hinshaw G., Nolte M. R., Odegard N., Page L., Spergel D. N., Weiland J. L., Wright E. L., Halpern M., Jarosik N., Kogut A., Limon M., Meyer S. S., Tucker G. S., Wollack E., 2003, *ApJS*, 148, 97
- Berkhuijsen E. M., Mitra D., Mueller P., 2006, *Astronomische Nachrichten*, 327, 82
- Bernardi G., Carretti E., Fabbri R., Sbarra C., Poppi S., Cortiglioni S., Jonas J. L., 2004, *MNRAS*, 351, 436
- Bernardi G., de Bruyn A. G., Brentjens M. A., Ciardi B., Harker G., Jelić V., Koopmans L. V. E., Labropoulos P., Offringa A., Pandey V. N., Schaye J., Thomas R. M., Yatawatta S., Zaroubi S., 2009, *A&A*, 500, 965
- Bernardi G., Harker A. G. d. B. G., Brentjens M. A., Ciardi B., Jelić V., Koopmans L. V. E., Labropoulos P., Offringa A., Pandey V. N., Schaye J., Thomas R. M., Yatawatta S., Zaroubi S., 2010, *ArXiv e-prints*
- Bolton J. S., Becker G. D., Wyithe J. S. B., Haehnelt M. G., Sargent W. L. W., 2010, *ArXiv e-prints*
- Bowman J. D., Morales M. F., Hewitt J. N., 2009, *ApJ*, 695, 183
- Brentjens M. A., de Bruyn A. G., 2005, *A&A*, 441, 1217
- Burn B. J., 1966, *MNRAS*, 133, 67
- Carozzi T. D., Woan G., 2009, *MNRAS*, 395, 1558
- Ciardi B., Madau P., 2003, *ApJ*, 596, 1
- Cooray A., 2004, *PhRvD*, 70, 063509
- Cordes J. M., Lazio T. J. W., 2002, *ArXiv Astrophysics e-prints*
- de Bruyn A. G., Katgert P., Haverkorn M., Schnitzler D. H. F. M., 2006, *Astronomische Nachrichten*, 327, 487
- de Bruyn G., Miley G., Rengelink R., et al., 1998, *WENSS. ASTRON*
- de Oliveira-Costa A., Tegmark M., Gaensler B. M., Jonas J., Landecker T. L., Reich P., 2008, *MNRAS*, 388, 247
- Di Matteo T., Ciardi B., Miniati F., 2004, *MNRAS*, 355, 1053
- Di Matteo T., Perna R., Abel T., Rees M. J., 2002, *ApJ*, 564, 576
- Fan X., Strauss M. A., Becker R. H., White R. L., Gunn J. E., Knapp G. R., Richards G. T., Schneider D. P., Brinkmann J., Fukugita M., 2006, *AJ*, 132, 117
- Field G., 1958, *Proceedings of the IRE*, 132, 240
- Field G. B., 1959, *ApJ*, 129, 536
- Gaensler B. M., Madsen G. J., Chatterjee S., Mao S. A., 2008, *Publications of the Astronomical Society of Australia*, 25, 184
- Gleser L., Nusser A., Benson A. J., 2008, *MNRAS*, 391, 383
- Han J., Wielebinski R., 2002, *Chinese Journal of Astronomy and Astrophysics*, 2, 293
- Harker G., Zaroubi S., Bernardi G., Brentjens M. A., de Bruyn A. G., Ciardi B., Jelić V., Koopmans L. V. E., Labropoulos P., Mellema G., Offringa A., Pandey V. N., Schaye J., Thomas R. M., Yatawatta S., 2009a, *MNRAS*, 397, 1138
- Harker G. J. A., Zaroubi S., Thomas R. M., Jelić V., Labropoulos P., Mellema G., Iliev I. T., Bernardi G., Brentjens M. A., de Bruyn A. G., Ciardi B., Koopmans L. V. E., Pandey V. N., Pawlik A. H., Schaye J., Yatawatta S., 2009b, *MNRAS*, 393, 1449
- Haslam C. G. T., Salter C. J., Stoffel H., Wilson W. E., 1982, *A&AS*, 47, 1
- Haverkorn M., Katgert P., de Bruyn A. G., 2003, *A&A*, 403, 1045
- Jelić V., Zaroubi S., Labropoulos P., Thomas R. M., Bernardi G., Brentjens M. A., de Bruyn A. G., Ciardi B., Harker G., Koopmans L. V. E., Pandey V. N., Schaye J., Yatawatta S., 2008, *MNRAS*, 389, 1319
- Komatsu E., Dunkley J., Nolte M. R., Bennett C. L., Gold B., Hinshaw G., Jarosik N., Larson D., Limon M., Page L., Spergel D. N., Halpern M., Hill R. S., Kogut A., Meyer S. S., Tucker G. S., Weiland J. L., Wollack E., Wright E. L., 2009, *ApJS*, 180, 330
- Labropoulos P., Koopmans L. V. E., Jelic V., Yatawatta S., Thomas R. M., Bernardi G., Brentjens M., de Bruyn G., Ciardi B., Harker G., Offringa A., Pandey V. N., Schaye J., Zaroubi S., 2009, *ArXiv e-prints*
- Landecker T. L., Wielebinski R., 1970, *Australian Journal of Physics Astrophysical Supplement*, 16, 1
- Morales M. F., Bowman J. D., Hewitt J. N., 2006, *ApJ*, 648, 767
- Oh S. P., Mack K. J., 2003, *MNRAS*, 346, 871
- Pacholczyk A. G., 1970, *Radio astrophysics. Nonthermal processes in galactic and extragalactic sources*. Freeman
- Page L., Hinshaw G., Komatsu E., Nolte M. R., Spergel D. N., Bennett C. L., Barnes C., Bean R., Doré O., Dunkley J., Halpern M., Hill R. S., Jarosik N., Kogut A., Limon M., Meyer S. S., Odegard N., Peiris H. V., Tucker G. S., Verde L., Weiland J. L., Wollack E., Wright E. L., 2007, *ApJS*, 170, 335
- Pen U.-L., Chang T.-C., Hirata C. M., Peterson J. B., Roy J., Gupta Y., Odegova J., Sigurdson K., 2009, *MNRAS*, 1240
- Platania P., Bensadoun M., Bersanelli M., de Amici G., Kogut A., Levin S., Maino D., Smoot G. F., 1998, *ApJ*, 505, 473
- Reich P., Reich W., 1986, *A&AS*, 63, 205
- , 1988, *A&AS*, 74, 7
- Reich W., 2006, *ArXiv Astrophysics e-prints*
- Reynolds R. J., 1990, in *IAU Symposium, Vol. 139, The Galactic and Extragalactic Background Radiation*, Bowyer S., Leinert C., eds., pp. 157–169
- Rogers A. E. E., Bowman J. D., 2008, *AJ*, 136, 641
- Rybicki G. B., Lightman A. P., 1986, *Radiative Processes in Astrophysics*. Wiley-VCH
- Santos M. G., Cooray A., Knox L., 2005, *ApJ*, 625, 575
- Schnitzler D., 2008, *PhD thesis, Leiden Observatory, Leiden University*, P.O. Box 9513, 2300 RA Leiden, The Netherlands
- Shaver P. A., Windhorst R. A., Madau P., de Bruyn A. G., 1999, *A&A*, 345, 380
- Spergel D. N., Bean R., Doré O., Nolte M. R., Bennett C. L., Dunkley J., Hinshaw G., Jarosik N., Komatsu E., Page L., Peiris H. V., Verde L., Halpern M., Hill R. S., Kogut A., Limon M., Meyer S. S., Odegard N., Tucker G. S., Weiland J. L., Wollack E., Wright E. L., 2007, *ApJS*, 170, 377
- Strong A. W., Moskalenko I. V., Reimer O., Digel S., Diehl R., 2004, *A&A*, 422, L47
- Sun X. H., Reich W., 2009, *ArXiv e-prints*
- Sun X. H., Reich W., Waelkens A., Enßlin T. A., 2008, *A&A*, 477, 573
- Theuns T., Schaye J., Zaroubi S., Kim T., Tzanavaris P., Carswell B., 2002a, *ApJL*, 567, L103
- Theuns T., Zaroubi S., Kim T., Tzanavaris P., Carswell R. F., 2002b, *MNRAS*, 332, 367
- Thomas R. M., Zaroubi S., Ciardi B., Pawlik A. H., Labropoulos P., Jelić V., Bernardi G., Brentjens M. A., de Bruyn A. G., Harker G. J. A., Koopmans L. V. E., Mellema G., Pandey V. N., Schaye J., Yatawatta S., 2009, *MNRAS*, 393, 32
- Waelkens A., Jaffe T., Reinecke M., Kitaura F. S., Enßlin T. A., 2009, *A&A*, 495, 697
- Wang X., Tegmark M., Santos M. G., Knox L., 2006, *ApJ*, 650, 529

- Webber W. R., Simpson G. A., Cane H. V., 1980, ApJ, 236, 448
Wieringa M. H., de Bruyn A. G., Jansen D., Brouw W. N., Katgert P., 1993, A&A, 268, 215
Wilson T. L., Rohlfs K., Hüttemeister S., 2009, Tools of Radio Astronomy. Springer

This paper has been typeset from a $\text{T}_{\text{E}}\text{X}/\text{L}^{\text{A}}\text{T}_{\text{E}}\text{X}$ file prepared by the author.